Towards a Radar/Radiometer Mode on the Dual-frequency, Dual-polarized Doppler Radar (D3R) System

Manuel A. Vega[1,2], V. Chandrasekar[2]

[1]NASA Goddard Space Flight Center, Greenbelt, MD

[2]Colorado State University, Fort Collins, CO

Abstract

- The dual-frequency, dual-polarized, Doppler radar (D3R) system was developed in support of the ground validation segment of the Global Precipitation Measurement (GPM) mission [1]. Although its main purpose is to provide active, Ku/Ka-band, dual-polarized measurements of precipitation, the design presents an opportunity to study its operation in an active/passive mode. The opportunity arises from use of solid-state transmitters employing a multi-frequency waveform and receiving system. Typically, a sequence of three pulses separated in frequency is transmitted to achieve its radar sensitivity and minimum range. However, one of the three pulses can be disabled with a tolerable decrease in sensitivity and its receive channel can be repurposed to support passive measurements.

- This work focuses on progress in the characterization of the Ku-band H polarized passive channel operating simultaneously with two active as a step towards the provision of brightness temperatures along with the other radar derived products. The methodology developed will be applied to the V polarized channel and Ka-band subsystem in the near future. The study consists on the analysis of the antenna performance, receiver architecture, transfer function and achievable number of independent samples, calibration method and preliminary observation analysis. All within the context of the instrument's current configuration and possible future improvements.

Fig. 1 D3R system deployed near Moclips, WA during the Olympic Mountain Experiment (OLYMPEx).

Antennas

- Within the dual-polarized radar realm of instrument design, antenna specifications are generally governed by spatial resolution, desired sensitivity, cross-polarized response performance and side-lobe levels among a few other important parameters. Many of these also apply to radiometers as well, however, beam efficiency and self-emission concerns are somewhat relaxed in the radar case. The following figures show efforts in an attempt to characterize the former.
- The antennas employed on the D3R system are prime focus parabolic reflectors. They are equipped with A-sandwich cone-shaped composite radomes to reduce wind loading and are equipped with a super-hydrophobic coating described in [2] to prevent the development of a water film therefore reducing the effects associated. Table 1 summarizes specifications and figure 5 shows the Ku and Ka-band antennas within the Goddard anechoic chamber during acceptance testing.

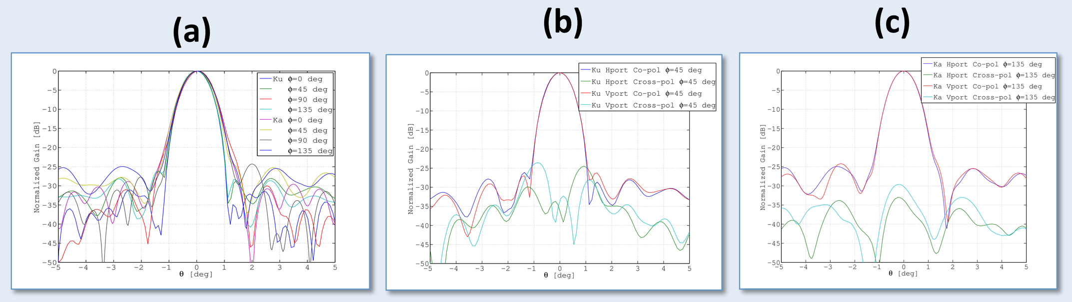

Fig. 1 (a) Ku, Ka-band co-polarized patterns, (b) Ku-band worst case phi plane co and cross-polarized patterns and (c) Ka-band worst case phi plane co and cross-polarized patterns.

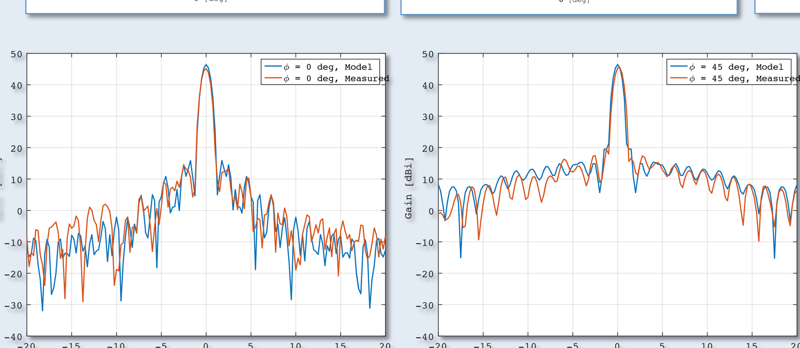

Fig. 2 Ku antenna measured and high resolution model overlay for phi = 0 and 45 deg cuts.

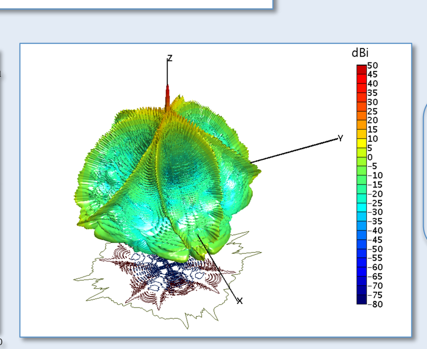

Fig. 3 Ku-band high resolution antenna model developed for further analysis.

$$\eta_b = \frac{\iint_{\text{main lobe}} f(\theta,\phi)\,d\Omega}{\iint_{4\pi} f(\theta,\phi)\,d\Omega}$$

Eq. 1 Beam efficiency

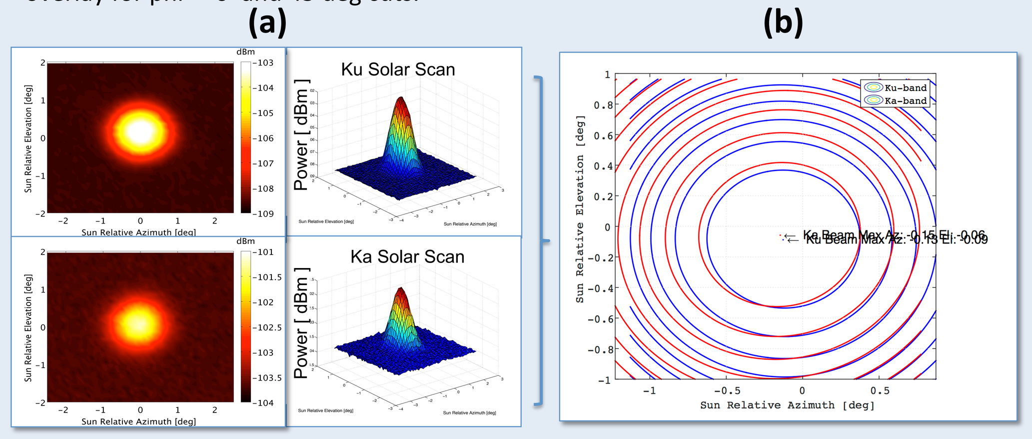

Fig. 4 Ku, Ka-band solar scan received power (a) and co-alignment results (b).

- Antenna co-alignment verification is performed routinely through solar scans.
- Adjustments are made, if needed to achieve co-alignment within 0.1 deg.
- Absolute pointing is calibrated from these scans.

Antennas (continued)

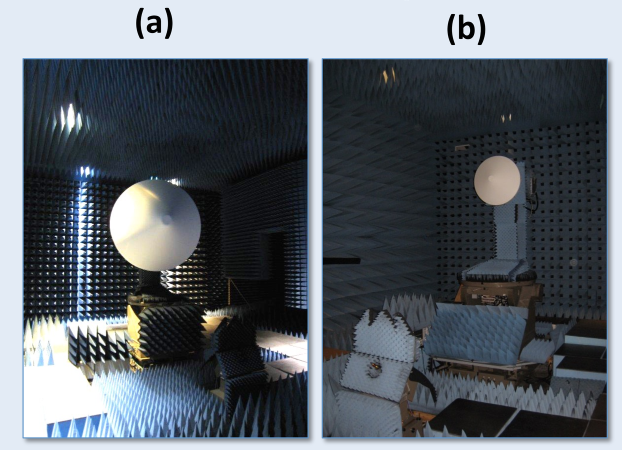

Fig. 5 Ku (a) and Ka-band (b) antennas during acceptance testing at the Goddard anechoic chamber.

Table 1 Antenna specifications

Parameter [Units]	Ku-band	Ka-band
Diameter [m]	1.8	0.71
Gain [dBi]	45.6	44.3
Half Power Beam width [deg]	0.86	0.90
Peak Sidelobe Level [dB]	~25	
On axis cross-pol [dB]	< -30	
Beam co-alignment [deg]	0.1	
Beam efficiency [%]*	~75.5	~67.5

* Beam efficiency estimate obtained from measured interpolated patterns using Eq 1.

Transmitter Receiver

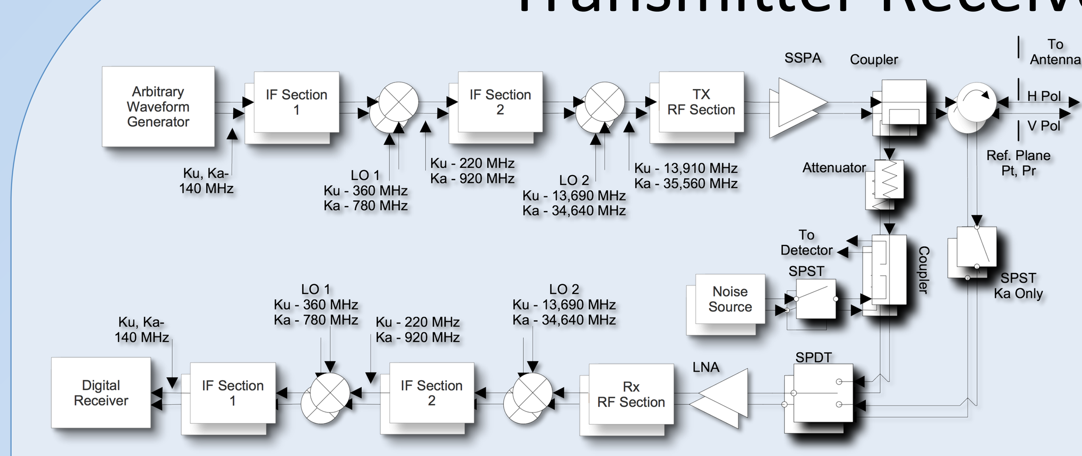

Fig. 6 Ku, Ka-band transmitter/receiver architecture.

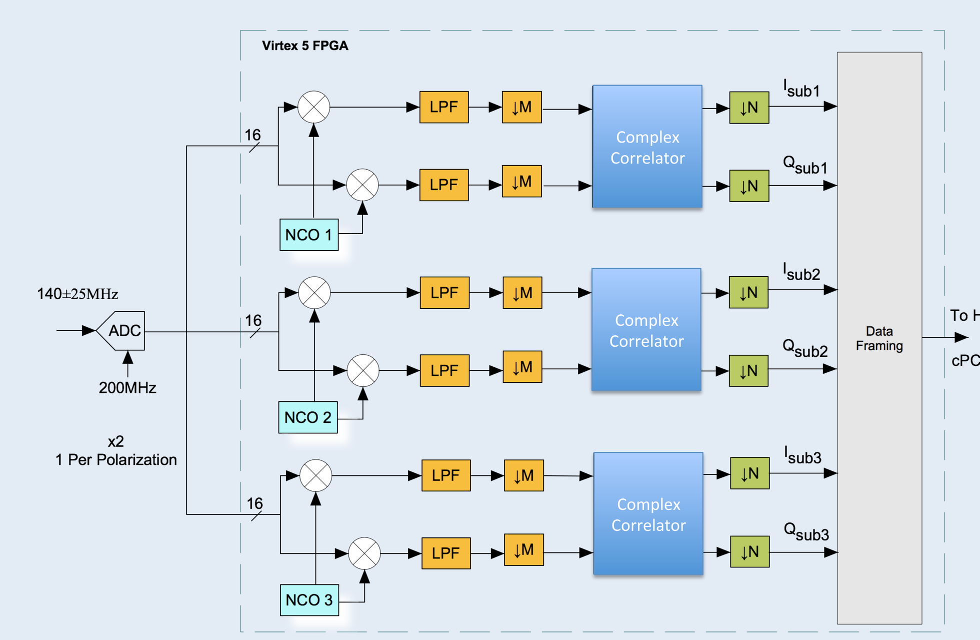

Fig. 7 Sub-banding digital receiver architecture.

Table 2 Transmitter receiver specifications.

Parameter [units]	Ku-band	Ka-band
Center Frequency [GHz]	13.91	35.56
Analog IF Bandwidth [MHz]	50	50
Transmitter Power [W]	200	40
Calibration Channel Isolation [dB]	>40	>40
Digital IF Bandwidth [MHz]	10	10
Noise Figure [dB]	4.6	6.3
Digital Sub-channels	3	3
Dynamic range [dB]*	~88	~87

* 1 MHz bandwidth, no noise correction

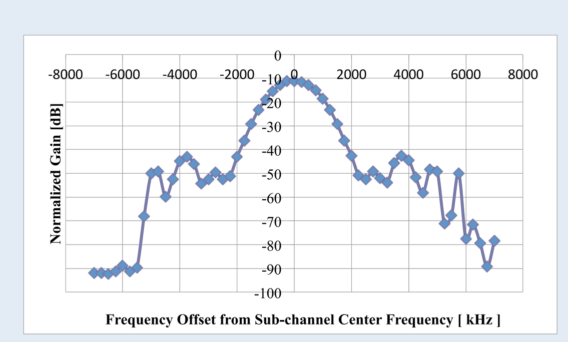

Fig. 8 Ku-band passive channel receiver transfer function used to determine pre-detection bandwidth and autocorrelation function.

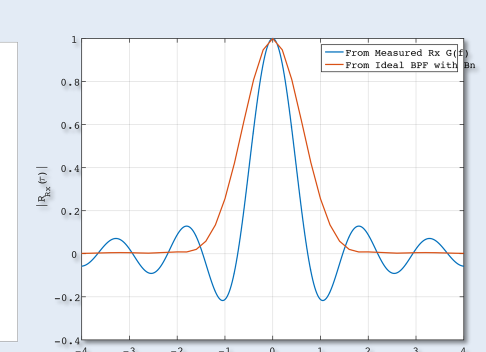

Fig. 9 Ku-band receiver autocorrelation function, from receiver measurements (red) and ideal bandpass filter with same *pre-detection bandwidth*.

$$B_{pre} = \frac{\left[\int_0^\infty H(f)\,df\right]^2}{\int_0^\infty H(f)^2\,df}$$

Eq. 2 Pre-detection bandwidth [3].

$$R_{xx}(\tau) = \int_{-\infty}^{\infty} H(f)e^{2\pi i f\tau}\,df$$

Eq. 3 Autocorrelation function.

- Approximately 23% drop in number of independent samples.

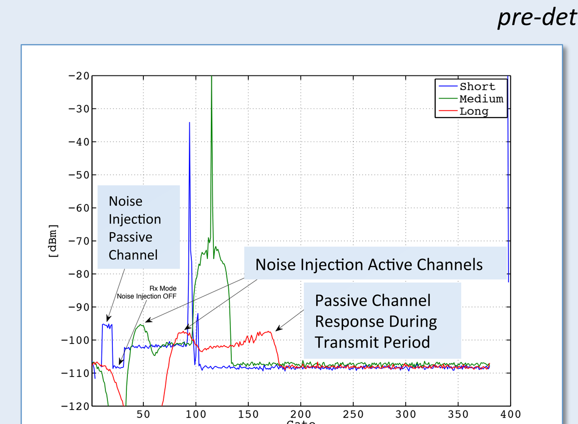

Fig. 10 Typical timing used during operations.

$$\Delta T = (T_A + T'_{rec})\sqrt{\frac{1}{B_{pre}\tau} + \left(\frac{\Delta G}{\bar{G}}\right)^2}$$

Eq. 4 Total power radiometer sensitivity with receiver gain fluctuations [4].

- Operating in total power mode with noise injection to track and correct receiver gain fluctuations.
- Biggest impact from NEDT is expected to come from receiver gain fluctuations.

Calibration Approach

$$\tau(m) = \ln\left[\frac{T_{MR} - T_{BG}}{T_{MR} - T_B(m)}\right]$$

Eq. 5 Optical thickness as a function of airmass m ($\sec(\theta_{zenith})$).

$$T_A = \frac{T_{out}}{G\Delta G} - T_{rec}$$

Eq. 6 Antenna temperature using measured receiver output and gain deviation. All other parameters estimated from past engineering measurements.

- End-to-end or tier 3 calibration as described in [5] is achieved from regular tip curve scans [6] during clear sky conditions.
- Eq. 5 is used to retrieve the offset in brightness temperature from a linear fit's intercept point.
- Fitting results are quality controlled based on R^2.
- For now, noise sources are assumed to be stable and changes in injected power are proportional to gain fluctuations.

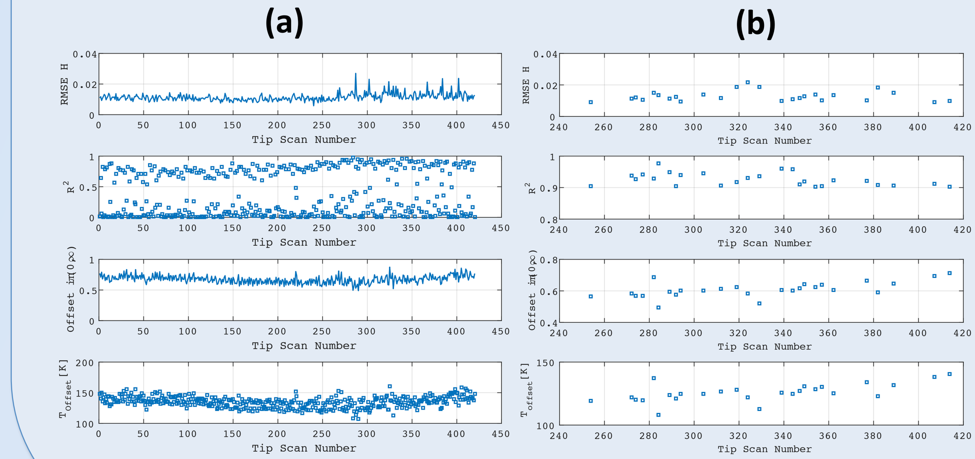

Fig 11 (a) Unfiltered and (b) filtered tip curve results.

- Fig 11 shows results for 420 tip curve scans collected during the OLYMPEx campaign in WA and spanning several weeks with and without filtering based on $R^2 = 0.90$.
- Best case obtained $R^2 = 0.9776$
- $T_{MR} = 273$ K was used as a placeholder until climatological dataset is obtained.
- Improvements in method are underway.

Preliminary Observations

- Finally, fig. 12 shows preliminary results obtained from cloud observations.
- Note the passive channel response to higher cloud reflectivities.
- Given that our own backscatter is a potential source for interference and that we're operating within an active band, kurtosis is being considered for RFI detection and also shown in fig 12 (c).
- Eq 7 was used to compute brightness temperatures corrected from tip curve calibration.
- Note the enhanced radar sensitivity stemming from the use of the passive channel to estimate the active channel noise.

$$T_B = \left[\frac{T_{out}}{G\Delta G} - T_{rec}\right] - T_{offset}$$

Eq. 7 Brightness temperature determined from tip calibration system offset.

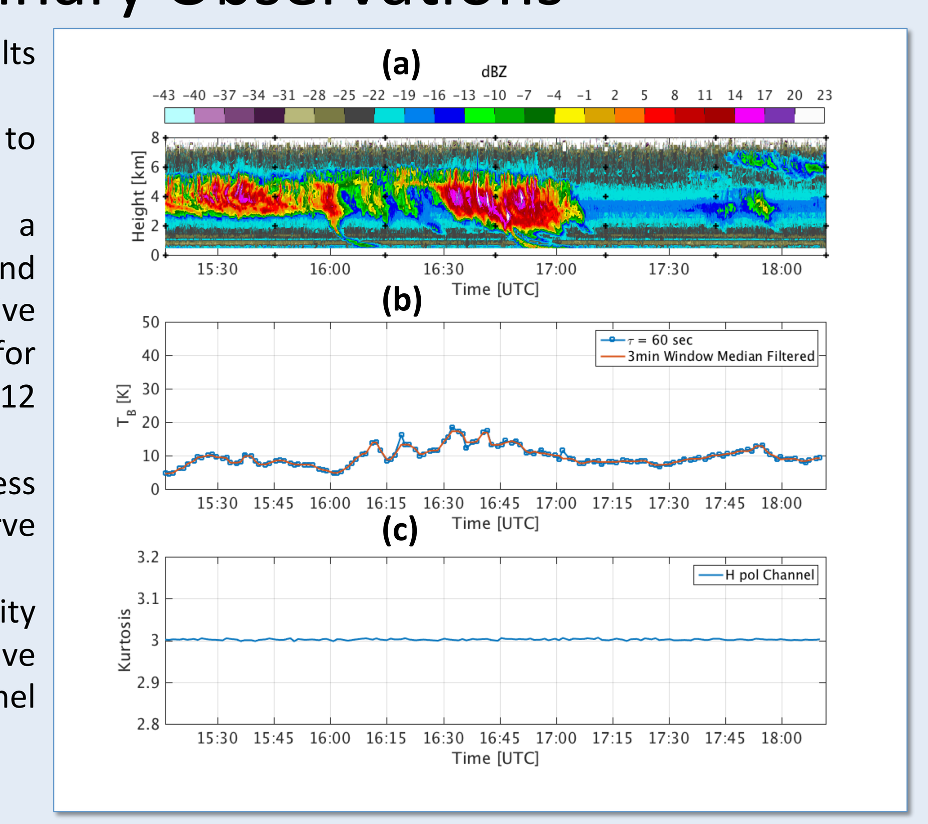

Fig. 12 Preliminary cloud measurement results collected at Wallops Flight Facility in zenith profiling mode. (a) Radar reflectivity, (b) brightness temperature and (c) kurtosis.

Concluding Remarks and Future Work

- Preliminary results shown are encouraging and show potential in achieving simultaneous active/passive measurements from the D3R platform. Further analysis and experimentation is planned to improve the tip curve calibration procedure, apply corrections based on sub-system temperatures and beam-efficiency effects.
- From a radar perspective, the passive channel is useful in providing a real-time noise estimation and correction method.
- Future system upgrades will aim at larger sub-channel bandwidths. Offset reflector antennas could potentially improve beam-efficiency.

Acknowledgements

This work was supported by the GPM GV program. Special thanks to Robert Beauchamp (CSU), Victor Marrero (GSFC), Aaron Dabrowski (GSFC), Mathew Schwaller (GSFC), Walter Petersen (MSFC), David Wolff (WFF), Jeffrey Piepmeier (GSFC) and many others that made this work possible.

References

[1] Vega, M., Chandrasekar, V., Carswell, J. Beauchamp, R., Schwaller, M., and Nguyen, C., Salient Features of the Dual-frequency, Dual-polarized, Doppler Radar for Remote Sensing of Precipitation, *Radio Science*, 2014.

[2] Salazar-Cerreño, Jorge L., Chandrasekar, V., Trabal, Jorge M., Siquera, Paul, Medina, Rafael, Knapp, Eric, McLaughlin, David J., A Drop Size Distribution (DSD)-Based Model for Evaluating the Performance of Wet Radomes for Dual-Polarized Radars, *Journal of Atmospheric and Oceanic Technology*, 2014

[3] Tiuri, M., Radio Astronomy Receivers, *IEEE Transactions on Antennas and Propagation*, 1964

[4] Ulaby, F., Moore, R., Fung, A., *Microwave Remote Sensing: Active and Passive Vol. 1*, Artech House

[5] Racette, P., Lang, R., Radiometer Design Analysis Based upon Measurement Uncertainty, *Radio Science*, 2005

[6] Han, Y., Westwater, E., Analysis and Improvement of Tipping Calibration for Ground-Based Microwave Radiometers, *IEEE Transactions on Geoscience and Remote Sensing*, 2000